

ANALYSIS OF ABNORMAL VIBRATIONS OF CRUDE OIL EFFLUX PUMPS USING ANSYS

TIANQI WANG

*Xian Shiyou University, Mechanical Engineering College, Xi'an, China, and
Xidian University, The School of Mechano-Electronic Engineering, Xi'an, China
Corresponding author, e-mail: wangtianqi@xsyu.edu.cn*

LEI XIE

Cementing Company Downhole Service Company CCDC, Chengdu, China

HONGSHENG YU, XIULIANG WEI

Changqing Oilfield Second Oil Transmission Office, Xianyang, China

PENGMIN DONG, TIANYI ZHAO

Xian Shiyou University, Mechanical Engineering College, Xi'an, China

In this study, abnormal vibrations of 1 pump fluid in a crude oil efflux station in the Changqing Oilfield was investigated. Kinetic simulation was applied to flow fields in the crude oil efflux pump using Ansys to determine trends of the impeller static pressure, speed, total pressure, wall pressure of the impeller, outlet pressure and pressure on the pump shell and to identify the reasons behind the abnormal vibrations. The results indicated that the axial vibration amplitude of the pump could be reduced from 1.3 mm down to 0.68 mm if the operation parameters of the external control oil pump were set as 2500-2550 r/min and 325-335 m³/h, respectively.

Keywords: abnormal vibrations, internal flow field, Ansys

1. Introduction

Impellers of a centrifugal pump are typically subject to highly complex 3D flows. Here, the fluid speed is distributed over several orders of magnitude; unidirectional flows and cross flow of multiphase flows are observed; separated flow, backflow and secondary flow also occur due to the effects of impeller rotation and surface curvature. As a result, fluid flows in an impeller can be extremely complicated (Shen, 2007). Considering the immaturity of existing testing methods, several researchers have used computational fluid dynamics (CFD) to numerically simulate characteristics of internal flows in the impeller of a centrifugal pump for impeller modeling and design, which has become an important research method in the modern pump technology (Chen *et al.*, 2014; Yu, 2008). Majidi (2005) solved an unsteady 3D viscous flow in the impeller and volute of a centrifugal pump using CFD methods. Benra and Dohmen (1966) investigated an unsteady flow field of a single-blade centrifugal pump using numerical simulation. The results showed that the lift increased in direct proportion with the flow. Boehning *et al.* (2011) investigated the effects of the volute structure on the radial force of a blood pump by using transient numerical methods. The results showed that a dual-volute structure could effectively reduce the radial force compared with the circumferential volute. Barrio *et al.* (2011) calculated the radial force of the impeller of a centrifugal pump under undesigned flow conditions by using a transient numerical method and found that the radial force was 40-70% of that under steady conditions, while the radial force under unsteady conditions was closer to the experimental

results. Mele *et al.* (2014) investigated correlation of vibrations and unsteady flows in a pump under different speeds using both experimental and simulation methods. The results showed that flow-induced vibrations increased with increasing pump speed and were significantly related to pump efficiency.

In this study, the speed and pressure variations were simulated, and by combining the simulation results with the vibration condition of the centrifugal pump during operation, a flow range that could reduce vibration was obtained to guide the actual production.

A crude oil pump group consists of feeding pumps, efflux pumps, heating furnaces, oil storage tanks, reverse feeding pumps and other components. The two feeding pumps and three efflux pumps were double-suction centrifugal pumps purchased from the Hunan Tane Ocean Pump Co., Ltd. (China). The oil pump had a lift of 480 m, a flow of 500 m³/h, a rated speed of 2980 r/min, a maximum allowed working pressure of 8.8 MPa, a bearing model of 7316B/DB, and a rated motor power of 800 kW. To increase the pump lift, 1 feeding pump worked in tandem with 1 and 2 efflux pumps during the operation of the pump group. The actual working speed and flow of the efflux pumps ranged from 2400 to 2750 r/min and about 350 m³/h, while the rated speed and flow of the efflux pumps were 2980 r/min and 500 m³/h, respectively.

The three efflux pumps at the oil efflux station were put into operation on September 15, 2015, and the accumulated operation time until the end of June 2019 was 23,835 hours for 1 efflux pump, 25,511 hours for 2 efflux pump and 23,509 hours for 3 efflux pump, all of which have been operating alternately for nearly four years. For 1 efflux pump, cavitation occurred during operation, the impeller in the pump shell had indications of being subjected to cavitation, and there was obvious crackling sound from the inside. Uninterrupted monitoring for the past five years indicated that vibration at the low-pressure end of 1 efflux pump has become increasingly large, and the transient vibration tested on February 24, 2020 exceeded 9.0 mm/s. After the mode of operation was adjusted using different methods, the vibration perpendicular to the axial direction at the low-pressure end of the pump often exceeded 7.1 mm/s.

With regard to vibrations of an oil pump, this paper proposed a rational speed and flow range using Ansys based on the change law of the flow field and fluid pressure in the pump, to guide the actual production and reduce the vibration amplitude of the pump so as to ensure unhindered production.

2. The pump model

2.1. Geometric parameters of the pump model

A double-suction centrifugal pump was used as the model in this study. This pump had a designed flow of $q_v = 500 \text{ m}^3/\text{h}$, designed lift of $H = 480 \text{ m}$, designed speed of $n = 2980 \text{ r/min}$, specific speed of $n_s = 40$, designed efficiency of $\eta = 78\%$, blade number of $z = 6$, impeller inlet diameter of $D_0 = 180 \text{ mm}$, impeller outlet diameter of $D_2 = 541 \text{ mm}$, and impeller outlet width of $b_2 = 21.1 \text{ mm}$. Additionally, $q_v = 357 \text{ m}^3/\text{h}$, and speed $n = 2554 \text{ r/min}$.

2.2. Meshing of the pump model

The centrifugal pump model was simplified using SolidWorks 2019 and fluid domains were selected in SpaceClaim. Figure 1 shows the established model.

The model consists of inflow runners, rotors, guide vanes, volutes, outflow runners and other components. To ensure the overall quality of the mesh and shorten the computational time, all the overflow components were divided using unstructured meshes in this paper. Each component was structurally divided into blocks to pre-generate the mesh, and by adjusting the distribution

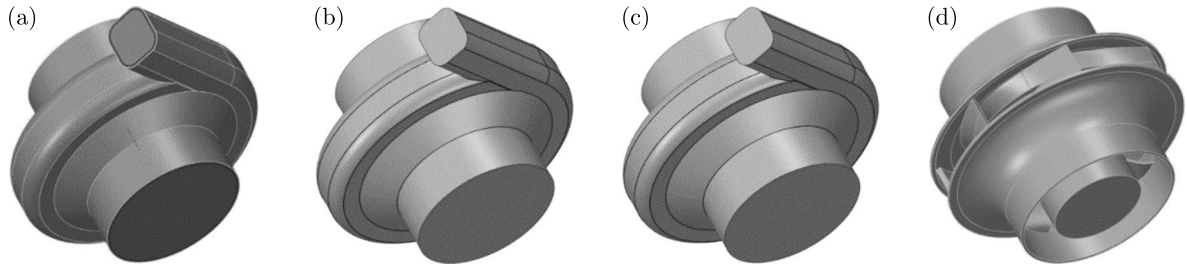


Fig. 1. 3D model of the centrifugal pump: (a) volute fluid domain, (b) pump shell fluid domain, (c) impeller fluid domain, (d) impeller

of nodes and the number of nodes, the mesh domain of each overflow component was encrypted in the targeted manner (Zhao *et al.*, 2005).

The boundary conditions were determined for meshing in FLUENT, with the impeller fluid having 956,000 elements and the shell fluid domain having 1.245 million elements. Figure 2 shows the developed mesh.



Fig. 2. Model meshing

2.3. Boundary conditions

Given the designed flow and lift of the target pump, the inlet boundary condition was set as the mass flow inlet, and the outlet boundary condition was set as a pressure outlet. Numerical simulation results were used to calculate the corresponding lift and efficiency. The rotating boundary was set as the rotor, the non-slip boundary condition was set as the wall, and the standard wall function was used for the near-wall region (Han *et al.*, 2004). Due to the complex working conditions of the pump station, and influenced by many factors such as pipelines, valves, feeding pumps and discharges, the measured data were averaged in this study. Table 1 lists the specific boundary conditions.

Table 1. Boundary conditions

Inlet pressure [(MPa)]	Flow rate at inlet [kg/s]	Speed [r/min]	Center-of-mass coordinates of impeller model	Gravitational acceleration [m/s ²]
0.6134	single inlet, 49.603, two inlets, 99.206	2554.44	$\bar{X} = -0.0541268$ $\bar{Y} = -0.0281454$ $\bar{Z} = 0.413535$	9.81

2.4. Selection of the turbulence model

The SST $k-\omega$ turbulence model is used to convert between the $k-\omega$ model for the near-wall region and the $k-\omega$ model for the far-field region using a blending function. It combines the accuracy of the $k-\omega$ model for calculating viscous flows in the near-wall region with the reliability of the $k-\omega$ model for calculating free flows in the far-field region. The advantage of this model is that it considers turbulent shear stresses and can obtain accurate results even when flow separation occurs. In this study, the SST $k-\omega$ turbulence model was chosen for computation. Herein, the pressure term adopted the second-order central difference format; the momentum term and the turbulent viscosity correction were computed using the second-order windward format. The speed and pressure in the flow field were coupled using the Simple algorithm (Wang, 2004).



Fig. 3. Boundary condition settings

Mass flow inlet conditions were used for the inlet, and the data were exchanged between the overflow components of the pump using interfaces. The inflow and outflow runner walls of the model pump and the cavity walls of the pump were set as stationary walls. The walls of the blade

and the impeller that rotate with the impeller were set as rotational boundaries. The no-slip boundary conditions were used for solid walls, and the standard wall function was used for near walls. The convection term was discretized using the second-order windward scheme, the diffusion term was discretized based on a central difference format with the second-order accuracy, and the speed and pressure were coupled by the Simple algorithm. To ensure convergence, the monitoring residual value was set to 10^{-5} . Figure 2 shows the developed mesh. The boundary conditions are set in Fig. 3.

2.5. Mesh-independent verification

To exclude the influence of the total number of meshes on the results, 56 sets of meshes with different amounts were divided for mesh-independent verification. The lift of the centrifugal pump was used as a dependent variable for the mesh-independent verification. When the lift fluctuation was less than 1%, the meshes were considered to meet the computational requirements. Meanwhile, by considering both the computational time and resources required for numerical computation, 2.2 million elements were finally selected as the computational requirement. Figure 4 shows the trend of curve change, between 2.1 and 2.3 it is gentle and stable, so 2.2 was selected.

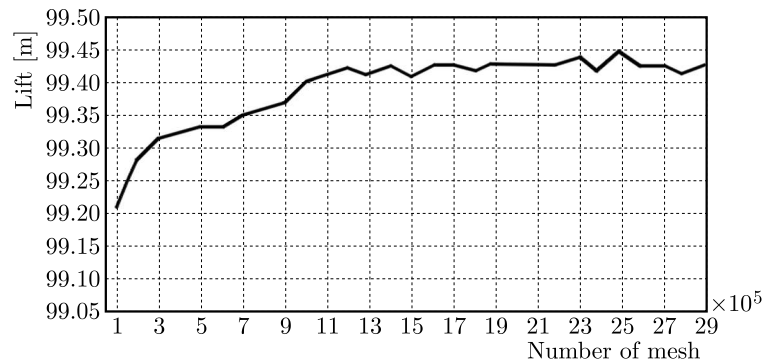


Fig. 4. Relationship between lift and mesh

3. Fluid analysis

3.1. Unstable flow characteristics in the centrifugal pump

A centrifugal pump comprises impellers and volutes. The complex structure and flow patterns result in the formation of unstable unsteady turbulence flows. When a centrifugal pump operates, the internal flows of the pump have many unstable flow characteristics, such as backflow at the impeller inlet, a wake-jet structure of the impeller outlet, and induced vibrations and noise. These unsteady flow characteristics determine the operating performance of the centrifugal pump.

3.1.1. Backflow

Backflow generally occurs at the inlet and outlet of the impeller. The backflow at the impeller inlet is mainly caused by an uneven force of high-speed rotating blades on the internal fluid. Due to the centrifugal force during operation, a pressure difference exists between the fluid flow at the outer edge of the inlet and the fluid in the inlet pipe near the shaft. The pressure at the outer edge is higher than that at the shaft, thus resulting in the fluid backflow from the impeller inlet to the inlet pipe (Zhu, 2008). Figure 5 shows the schematic of the backflow.

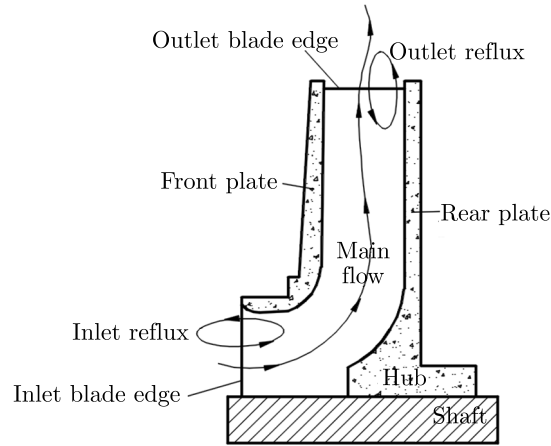


Fig. 5. Schematic of backflows at the inlet and outlet of the centrifugal pump

3.1.2. Wake-jet structure

As mentioned above, the flow rate near the blade pressure surface accelerates, while the fluid flow near the blade suction surface slows down, resulting in a wake-jet structure. A jet zone with a relatively high flow rate and almost zero viscosity exists near the blade pressure surface, while the wake zone with a relatively low flow rate is near the blade suction surface (Zhang, 2001). Figure 6 shows the wake-jet structure.

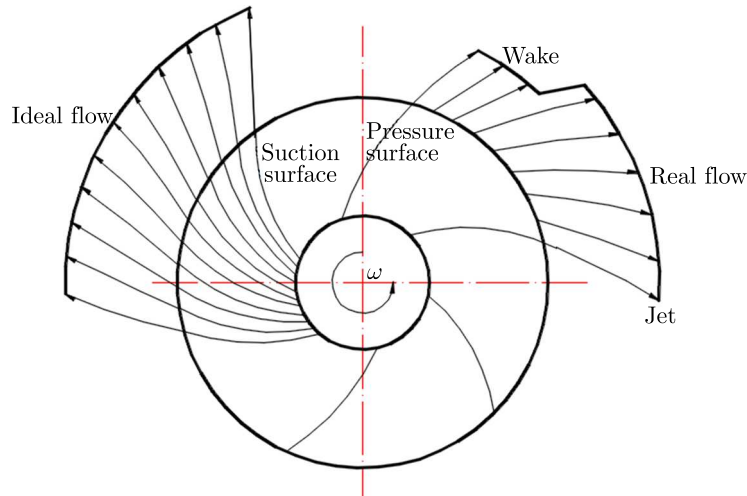


Fig. 6. Wake-jet structure in the sub-impeller

3.2. Analysis of streamlines

Fluent has a wide range of analytical functions and a series of flow models including those for a steady flow, laminar flow, turbulent flow and unsteady flow. The computation and display of streamlines is a fundamental technique in the visualization of flow fields. In this study, the CFD computational mesh was divided into tetrahedral cells first, and the topological relation between the adjacent tetrahedra was set. Subsequently, the “compass” method based on the tetrahedral side method was used for fast point location, and an adaptive step numerical integration method was used to trace the streamlines directly in the physical space. By doing so, the conversion between the physical space, computational space and resulting errors were avoided, and the accuracy and efficiency of streamline tracing were improved (Zhang, 2007). After the computation was completed, Ansys was used to generate streamlines.

Figure 7 shows the distribution of streamlines in the flow field. As observed, the fluid flows in from the fluid domain inlet, and at this point, the streamline is distributed in a regular and orderly manner. After rotation of the impeller, the flow pattern of the streamline changes, and the streamline moves in a spiral shape and flows out from the outlet. The fluid in the pump cavity accelerates, and the fluid in the impeller shows a gradient distribution in terms of the flow rate. Since diameter of the outlet is smaller than that of the inlet, the flow speed at the outlet is significantly higher than that at the inlet. Additionally, the presence of a wake-jet structure and boundary layer separation in the flow runner will lead to increased hydraulic losses, low pump efficiency, and even vibrations.

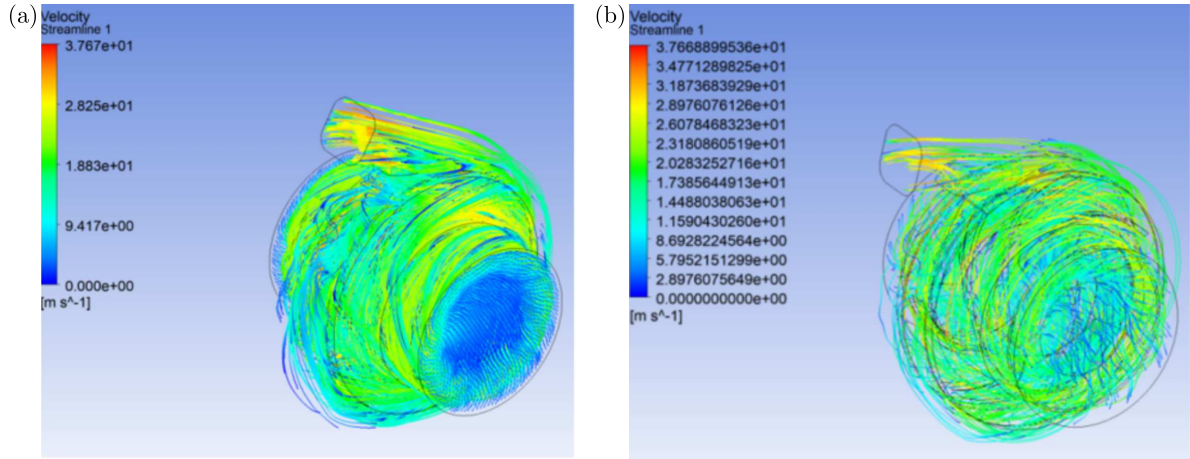


Fig. 7. Distribution of streamlines in the flow field: (a) distribution of the encrypted streamline, (b) distribution of the unencrypted streamline

3.3. Numerical analysis of the impeller

3.3.1. Static pressure

Figure 8 shows the distribution of impeller pressure. As observed, the absolute pressure at the root of the blade in the suction inlet section is lower than that at the blade edge, and the pressure at this position is the same as the outlet pressure of the feeding pump (about 6.4 kPa), which facilitates normal suction of the fluid flowing out from the feeding pump. The pressure at the blade edge is 1.3 MPa, and the pressure gradually increases from the root to the edge of the blade. Given that the blade edge and discharge outlet are closely positioned, the fluid can flow smoothly from the suction inlet to the discharge outlet under low-pressure suction. In summary, the impeller shows good suction and discharge capacity.

3.3.2. Speed

Figure 9 shows the distribution of impeller speed. As observed, the blade edge speed increases from the root to the end surface with a maximum speed of 75.1 m/s, and the speed at the suction inlet section is lower than that at the blade edge. The inlet flow rate is calculated as

$$v = \frac{Q}{S} = \frac{357.14}{3600 \cdot (0.09)^2 \cdot \pi} = 3.90 \frac{\text{m}}{\text{s}} \quad (3.1)$$

where Q is the average inlet flow at the centrifugal pump and S is the area of the inlet section with a diameter of 180 mm.

Therefore, the fluid with a relatively low flow rate can be significantly increased after flowing through the impeller. Nevertheless, due to the influence of the secondary flow in the impeller

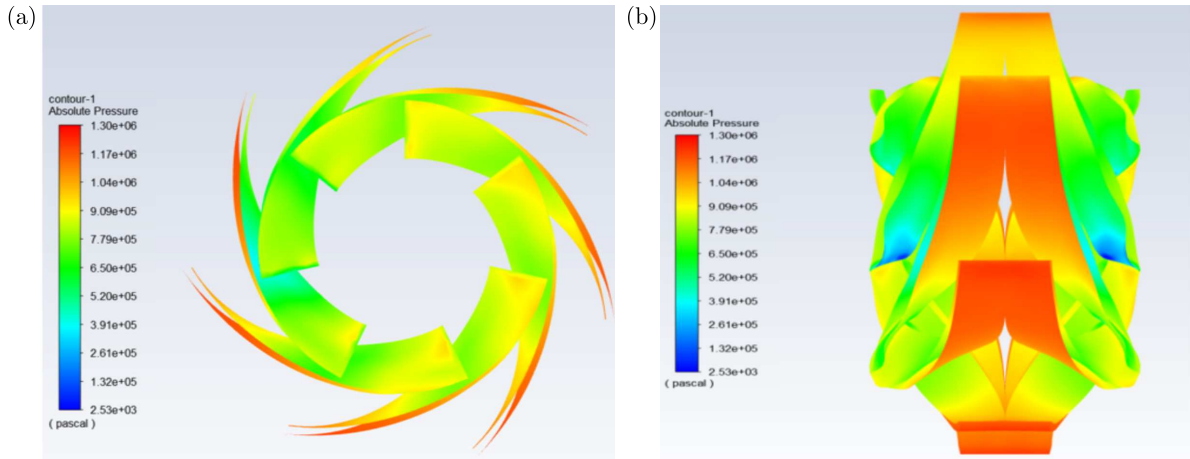


Fig. 8. Distribution cloud of impeller pressure: (a) front view, (b) side view

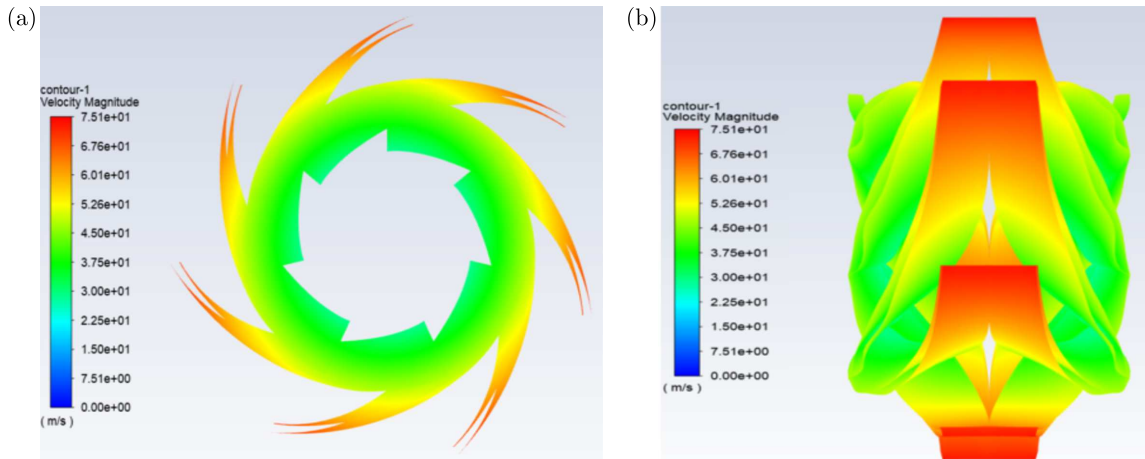


Fig. 9. Distribution cloud of impeller speed: (a) front view, (b) side view

flow runner, high-energy fluid microclusters are clustered at the blade pressure surface, which accelerates the fluid flow rate and thus reduces the possibility of boundary layer separation at the blade pressure surface. On the other side, the low-energy fluid microclusters enter the boundary layer near the suction surface of the blade, which reduces the flow rate near the suction surface, makes the boundary layer thicker and intensifies boundary layer separation at the suction surface of the blade (Wang *et al.*, 2022), which also becomes a triggering factor for pump vibrations.

3.3.3. Total pressure

Figure 10 illustrates the distribution of total pressure on the impeller.

As observed, the total pressure at the impeller blade surface is higher than that at the blade edge and shows an increasing trend from the root to the edge of the blade. Since the total pressure is the sum of static pressure and dynamic pressure, the dynamic pressure at the blade edge is higher than that at the root and its value is the highest, which is also consistent with the trend of speed distribution. The lower part of Fig. 10b shows that the pressure at the outlet is much higher than in other parts after the fluid flows across the impeller of the centrifugal pump. As shown in Fig. 10a, the work done by the blade on the fluid is not uniform, boundary layer separation occurs in the fluid in the impeller flow runner, and a separation vortex is formed in the flow runner. Boundary layer separation may cause vibrations, thus leading to low pump efficiency.

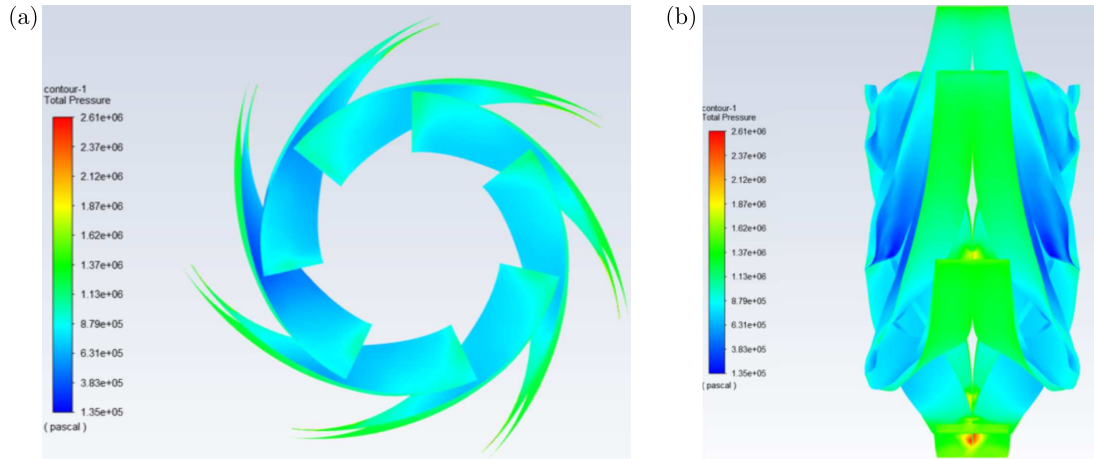


Fig. 10. Distribution cloud of total pressure on the impeller: (a) front view, (b) side view

3.3.4. Analysis of impeller inner wall

Figure 11 shows the distribution of the impeller inner wall pressure. As observed, the pressure distribution in the inner profile of the impeller is basically the same as that in the blade. Since the blade pressure distribution may be described in terms of absolute pressure, the outer profile is described in terms of the surface pressure (static pressure). As observed, the maximum and minimum pressures were 1.2 MPa and 4.0 kPa, respectively. This is partly a result of the combined effect of the impeller centrifugal force and the lifting force. The center of the impeller is the suction zone where the pump sucks the fluid, and the edge is the discharge zone for lifting the liquid pressure for discharge, which forms the work done in the fluid (Chu *et al.*, 2009).

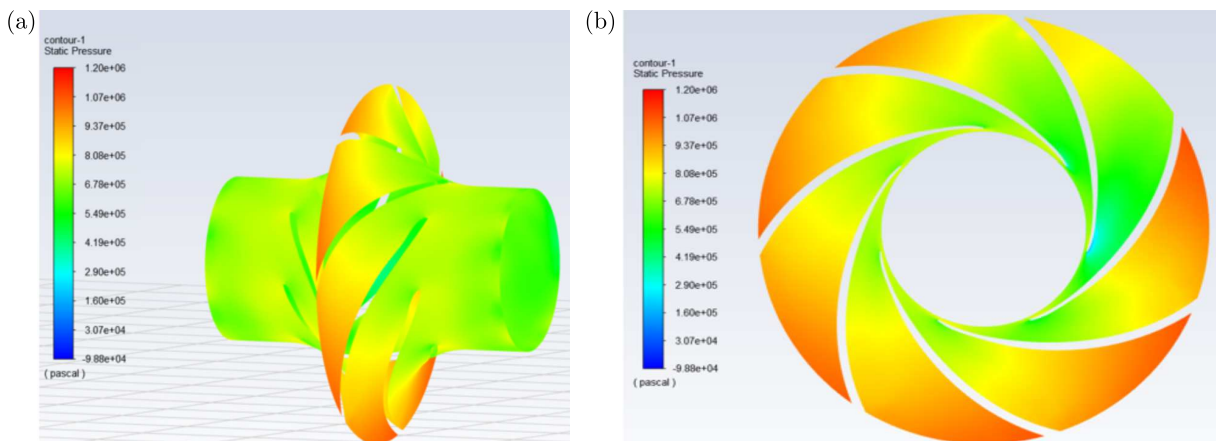


Fig. 11. Distribution cloud of pressure on the inner wall of the impeller

3.3.5. Pressure on the inner wall of the pump

Figure 12 shows the distribution of pressure on the inner wall of the pump. As observed, the maximum and minimum pressures were 1.2 MPa and 4.0 kPa, respectively. This is partly a result of the combined effect of the impeller discharge pressure and the pump shell. Thus, as the impeller radius increases, the pressure also increases, while the local pressure increases significantly due to the outlet backflow.

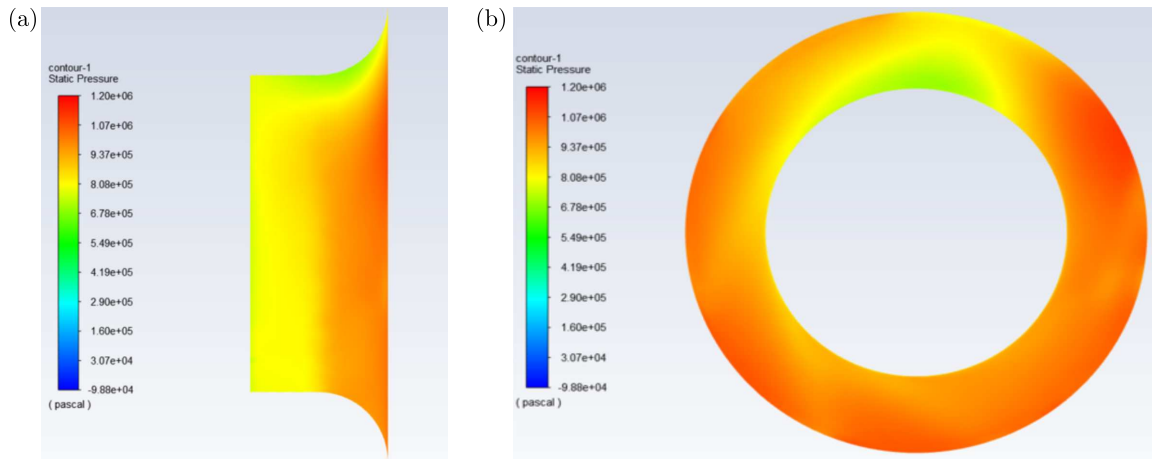


Fig. 12. Distribution cloud of pressure on the inner wall of the pump

3.3.6. Outlet analysis

Figure 13 shows the distribution of the efflux pump outlet pressure. The centrifugal rotation and backflow at the discharge outlet cause backflow near the bottom of the pump cavity. As a result, the bottom has a relatively low flow rate due to the impact of speed and pressure, while the centrifugal force at the top is relatively high, resulting in higher kinetic energy and higher total pressure at the top than at the bottom (Archard, 1953). The outlet pressure was calculated to be 1.3 MPa according to the surface average. The backflow at the impeller outlet is due to the combined effect of non-uniform fluid flows at the outlet and turbulent flows in the volute. The absolute speed of a portion of the fluid is greater than the flow rate in the volute, so this part of the fluid will hit the fluid in the volute with a relatively high kinetic energy. This fluid will be subjected to secondary work in the impeller and will consume more energy, while the flow rate of the rest of the fluid will be lower and will be pressed back into the impeller. Thus, a severe backflow may induce pump vibrations and lead to low pump efficiency.

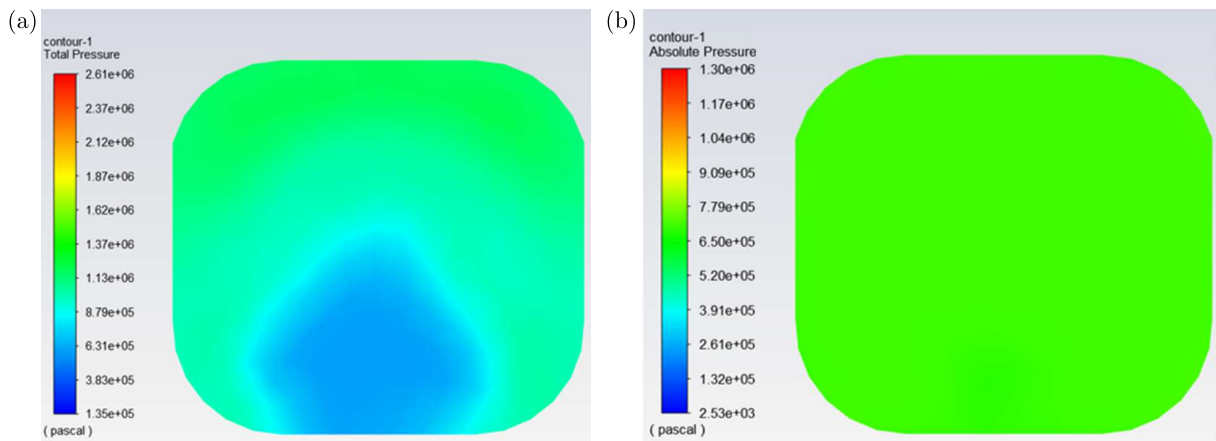


Fig. 13. Distribution cloud of outlet pressure of the output pump

3.3.7. Analysis of the pump shell

Figure 14 shows the distribution of pressure on the pump shell. The center of the pump shell is influenced by the centrifugal lifting force, cavity volume and outlet diameter. The pressure at the center is significantly higher than the suction inlets on both sides, and the pressure decreases

symmetrically along the center surface under the influence of the pump impeller, eventually dropping down to the inlet suction pressure (Chen *et al.*, 2017). The fluid flows in from the inlet negative pressure zone (pressure is relatively low) and flows out of the pump cavity along the tangential direction after the work done by the impeller. Figures 15 and 16 show the cross-section of the shell.

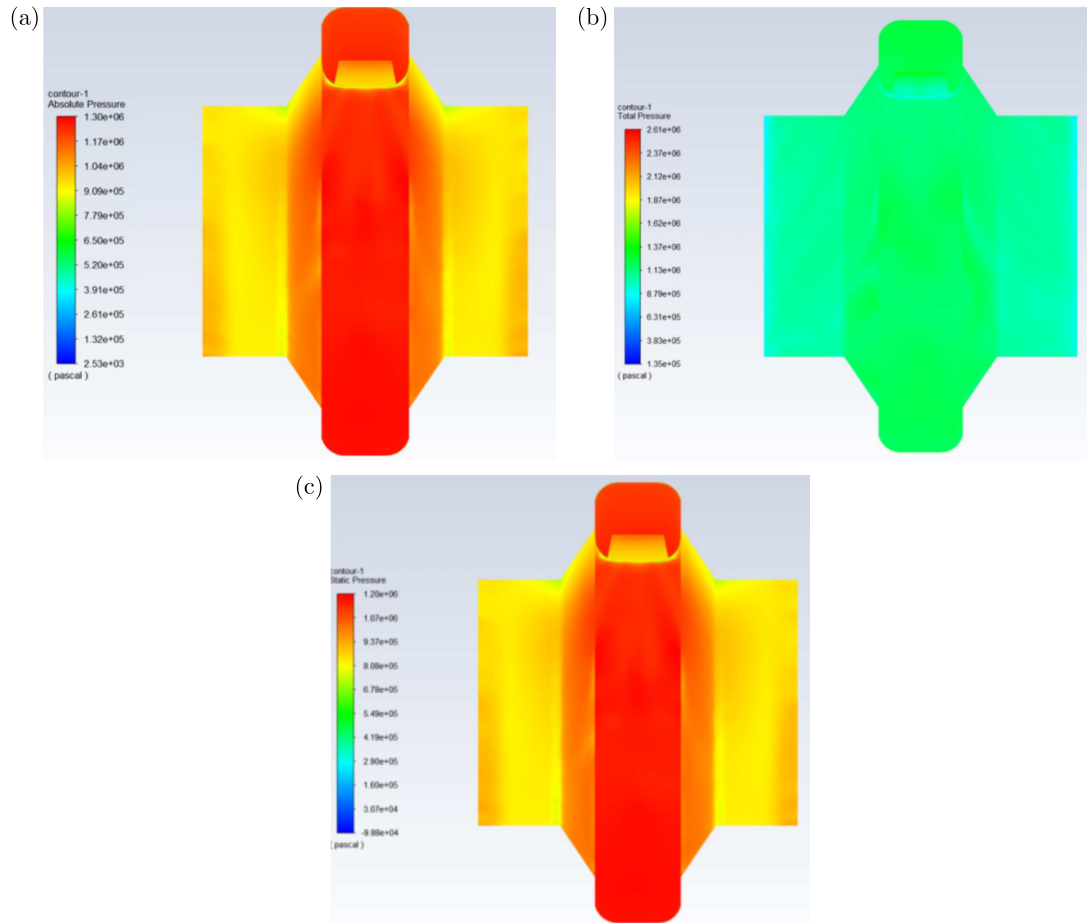


Fig. 14. Distribution cloud of pressure on the pump shell: (a) absolute pressure, (b) total pressure, (c) static pressure

After the centrifugal pump is started, the pump shaft will drive the impeller to facilitate a high-speed rotational movement, forcing the pre-filled fluid between the blades to rotate. Under the action of the inertial centrifugal force, the fluid moves radially from the center of the impeller to the outer circumference. In the process of flowing through the impeller, the fluid will gain energy, resulting in an increased static pressure energy as well as an increased flow rate. When the fluid flows out of the impeller into the pump shell, the flow rate decelerates with a gradual expansion of the flow runner in the shell. In this process, a part of the kinetic energy is converted into static pressure energy, and finally, the fluid flows into the discharge pipe along the tangential direction. While the fluid is thrown from the center of the impeller to the periphery, a low-pressure zone will be formed in the center of the impeller, and the fluid is sucked into the center of the impeller under the action of the total potential energy difference between the liquid surface in the storage tank and the center of the impeller. Depending on continuous operation of the impeller, the liquid will be continuously sucked and discharged. The mechanical energy absorbed by the liquid in the centrifugal pump may be observed in the form of an increase of static pressure energy (Blais *et al.*, 2016; Li *et al.*, 2019).

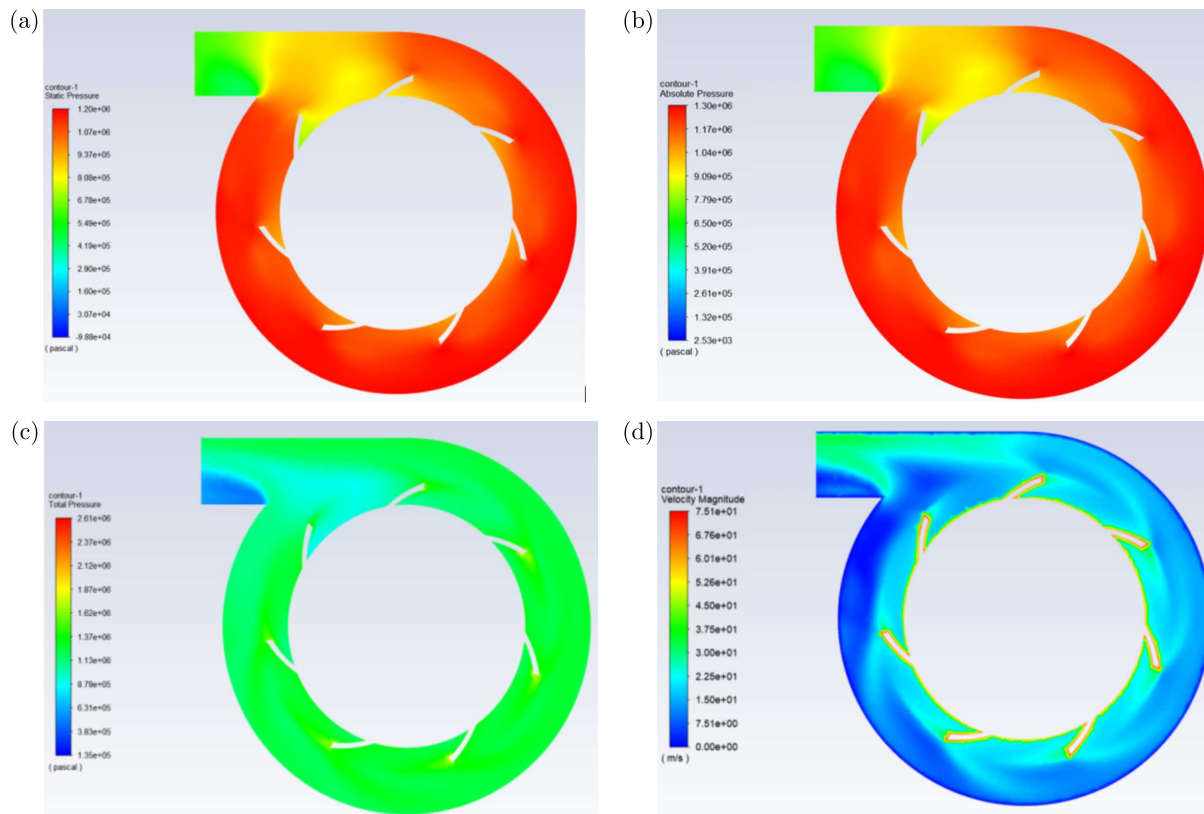


Fig. 15. Vertical center cross-section of the pump shell: (a) distribution of static pressure, (b) distribution of total pressure (difference between the pressure and the static pressure is one atmosphere), (c) total pressure, (d) speed vectorgraph

Based on the results of the simulation analysis of pressure variation, the following operational verification parameters were obtained (Table 2). The results indicated that when the speed and flow rate of the efflux pump was 2300-2550 r/min and 325-335 m³/h, the maximum vibration value was less than 1.3 mm/s, respectively.

Table 2. 1 pump verification parameters under actual working conditions (high-pressure end)

1 efflux pump [r/min]	Output volume [m ³ /h]	Axial vibration [mm]
2519	331	0.68
2575	334	0.91
2325	332	1.05
2475	333	1.03
2525	331	1.08
2550	354	1.18
2450	355	1.1
2400	356	1.3

4. Conclusions

Based on the results of the simulation analysis of pressure variation, the following operational verification parameters were obtained.

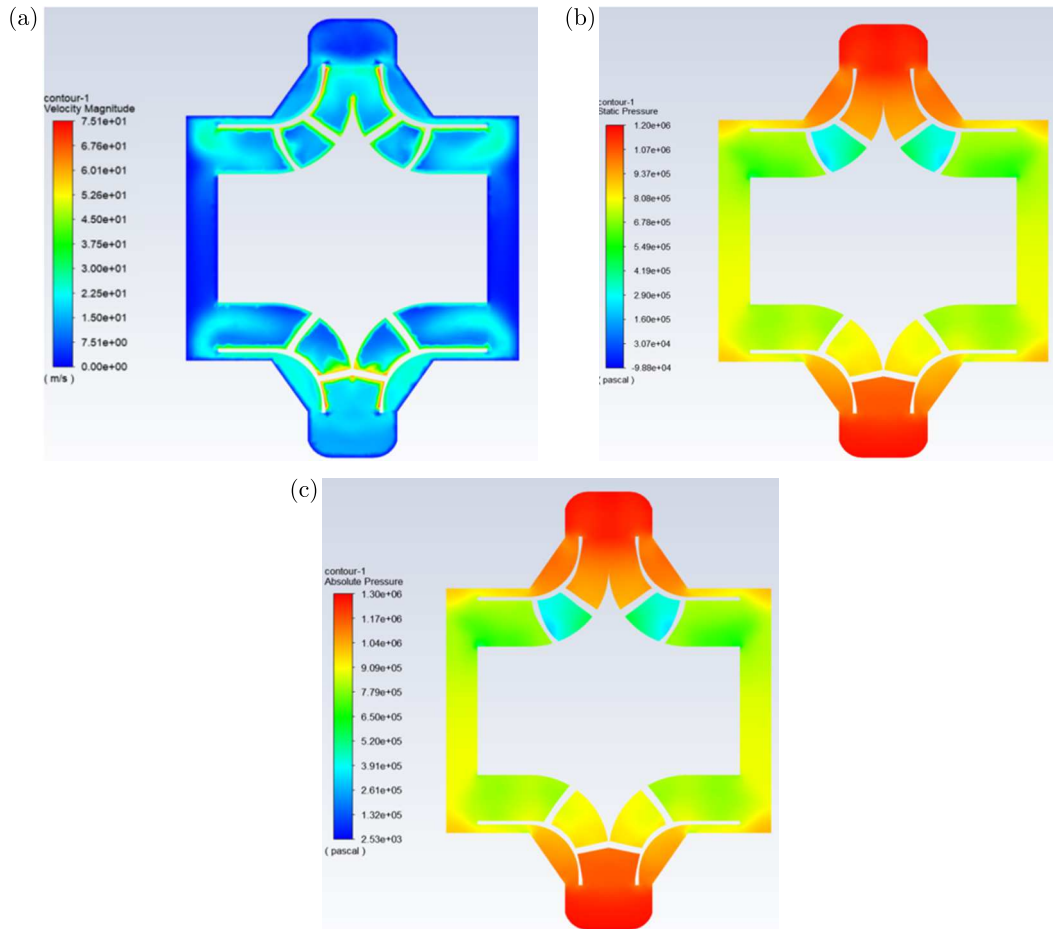


Fig. 16. Horizontal center cross-section of the pump shell: (a) speed vectorgraph, (b) static pressure, (c) absolute pressure

In summary, the pump axial vibration was minimized down to 0.68 mm/s, and the speed and output volume of 1 efflux pump were 2519 r/min and 331 m³/h, respectively. The abnormal vibrations of the efflux pump during operation were investigated by kinetic simulation of the flow fields in the efflux pump using Ansys. A rational speed and flow rate range through parameter verification was proposed to guide the current production. The results indicated that when the speed and flow rate of the efflux pump was 2500-2550 r/min and 325-335 m³/h, respectively, the vibrations of the efflux pump could be significantly decreased. The vibration value was reduced to 1.3 mm/s, which is 85.6% lower than the original instantaneous needle movement (9 mm/s) and less than 4.5 mm/s allowable for pump vibration. The normal production can be guaranteed.

Acknowledgment

The research was supported by Shaanxi Natural Science Basic Research Program (2022JM-150).

References

1. ARCHARD J.F., 1953, Contact and rubbing of flat surfaces, *Journal of Applied Physics*, **24**, 8, 981-988
2. BARRIO R., FERNÁNDEZ J., BLANCO E., PARRONDO J., 2011, Estimation of radial load in centrifugal pumps using computational fluid dynamics, *European Journal of Mechanics - B/Fluids*, **30**, 3, 316-324

3. BENRA F.K., DOHMEN H.J., 1966, Investigation on the time-variant flow in a single-blade centrifugal pump, *Louisiana History the Journal of the Louisiana Historical Association*, **7**, 3, 207-220
4. BLAIS B., LASSAIGNE M., GONIVA C., FRADETTE L., BERTRAND F., 2016, Development of an unresolved CFD DEM model for the flow of viscous suspensions and its application to solid-liquid mixing, *Journal of Computational Physics*, **318**, 201-221
5. BOEHNING F., TIMMS D.L., AMARAL F., OLIVEIRA L., GRAEFE R., HSU P.-L., SCHMITZ-RODE T., STEINSEIFER U., 2011, Evaluation of hydraulic radial forces on the impeller by the volute in a centrifugal rotary blood pump, *Artificial Organs*, **35**, 8, 818-825
6. CHEN G.M., SCHOTT D.L., LODEWIJKS G., 2017, Sensitivity analysis of DEM prediction for sliding wear by single iron ore particle, *Engineering Computations*, **34**, 6, 2031-2053
7. CHEN J.Q., YU J.C., LIU M.L., 2014, *Ansys Fluent Technical Foundation and Engineering Application* (in Chinese), Beijing, China Petrochemical Press, 11-20
8. CHU K.W., WANG B., YU A.B., VINCE A., 2009, CFD-DEM modelling of multiphase flow in dense medium cyclones, *Powder Technology*, **193**, 3, 235-247
9. HAN Z.Z., WANG J., LAN X.P., 2004, *Example and Application of Fluid Engineering Simulation*, Beijing: Beijing Institute of Technology Press, 15-60
10. LI Y., LIU S., HU X., 2019, Research on rotating speed's influence on performance of Deep-Sea lifting motor pump based on DEM CFD, *Marine Georesources and Geotechnology*, **37**, 8, 979-988
11. MAJIDI K., 2005, Numerical study of un-steady flow in a centrifugal pump, *Journal of Turbomachinery*, **127**, 2, 363-371
12. MELE J., GUZZOMI A., PAN J., 2014, Correlation of centrifugal pump vibration to unsteady flow under variable motor speed, *Mechanics and Industry*, **15**, 6, 525-534
13. SHEN Z.Z., 2007, *Analysis and Numerical Simulation of Liquid-Solid Two-Phase Flow in Radial Impeller* (in Chinese), Changsha University of Technology, Changsha, 23-40
14. WANG F.J., 2004, *Computational Fluid Dynamics Analysis*, Beijing: Tsinghua University Press, 23-50
15. WANG T.T., ZHI J.C., YANG J.R., XIE R.Z., YU L.M., CUI N.B., 2022, Numerical simulation of flow field and wear in centrifugal pump based on CFD-DEM, *Journal of Hunan Agricultural University (Natural Sciences)*, **48**, 2, 235-241
16. YU Y., 2008, *Fluent Introduction and Advanced Tutorial* (in Chinese), Beijing Institute of Technology Press, 25-60
17. ZHANG J.F., 2007, *Study on Numerical Prediction and Design Method of Full Flow Field of Centrifugal Pump with Splitter Blades*, Jiangsu: Jiangsu University, 100-152
18. ZHANG K.W., 2001, *Principles of Fluid Mechanics*, China Machine Press, 125-160
19. ZHAO Q.S., LI C.H., WANG B., 2005, Three-dimensional modeling design for centrifugal spiral casing based on Pro/E (in Chinese), *Journal of Shenyang Agricultural University*, **36**, 2, 241-243
20. ZHU Z.C., 2008, *Theory and Design Application of Low Specific Speed High Speed Centrifugal Pump*, Beijing: China Machine Press, 60-100